Supporting Information for "Inferring the Mean Thickness of the Outer Ice Shell of Enceladus from Diurnal Crustal Deformation"

Alexander Berne[1], Mark Simons[1], James Tuttle Keane[2], Ryan S. Park[2]

[1]California Institute of Technology, Pasadena, CA 91125 USA

[2]Jet Propulsion Laboratory, California Institute of Technology, Pasadena, CA 91109 USA

Contents of this file

1. Text S1

2. Figures S1 to S8

Introduction

In S1, we describe the governing equations for our tidal loading boundary value problem and our solution method (1.1), benchmark our solutions against analytic and numerical tidal loading models (1.2), and verify that results on models with heterogeneities are not subject to inaccuracy due to our choice of mesh sizing parameters (1.3) or our choice of weak-zone elastic moduli (1.4). We also investigate the extent that structural heterogeneities that induce non degree-2 harmonics in radial displacement fields (1.5), examine whether the mean ice thickness tracked in this study (i.e., $\tilde{d}_{ice}$) approximates the thermal thickness of Enceladus's ice shell (1.6), and illustrate the impact of structural heterogeneities on horizontal displacements at Enceladus (1.7).

Text S1

1.1 Governing Equations

1.1.1.1 Strong Form of the Equation of Motion

Following Aagaard et al. (2007), we formulate and solve a boundary value problem appropriate for tidal loading. We start by defining the strong form of the quasi-static equation of motion for a geometry with fault surfaces:

$$\sigma_{ij,j} + f_i = 0 \text{ in } W \tag{1a}$$

$$\sigma_{ij} n_j = T_i \text{ on } S \tag{1b}$$

where i describe cartesian directions i for a body subject to stresses σ_{ij} and specific forces f_i over the volume W, T_i describes tractions on all surfaces S, and n_j is the vector normal to S. We subdivide S into the surface at the outer domain boundary S_0, the surface at the inner (i.e., ice-ocean) domain boundary S_{int}, and surfaces corresponding to fault interfaces S_f of our geometry.

1.1.1.2 Constitutive Relation for Elasticity

We write a constitutive relation for elasticity (i.e., Hooke's law) using the rank-4 stiffness tensor C_{ijkl} to map displacements u_{kl} to stresses σ_{ij}. We assign parameters in C_{ijkl} that are appropriate for linear isotropic material with a shear modulus G and bulk modulus μ (see Table 1 of the main text; the symbol , denotes derivative with respect to a direction):

$$\sigma_{ij} = \frac{1}{2} C_{ijkl}(u_{k,l} + u_{l,k}) \tag{2}$$

1.1.1.3 Tidal Loading

Building on the procedure of Souček et al. (2016) (see S1), we formulate three components of tidal loading: 'body', 'ocean', and 'topographic' forces. We additionally treat a

fourth 'self-gravitational' force for this work. As per Newton's second law, the body force f_i^b arising from diurnal tides is the gradient of the driving potential (i.e, see Equation 7 of the main text) scaled by ice density ρ_{ice} ($\mathbf{e}^i$ denotes the unit vector parallel to the evaluated direction):

$$f_i^b = \rho_{ice}(\nabla V) \cdot \mathbf{e}^i \tag{3}$$

The ocean force is a traction T_i^o on S_{int} which scales the driving potential V with ocean density ρ_w ($\mathbf{e}^s$ denotes the unit vector perpendicular to the surface of the geometry):

$$T_i^o = \rho_w V(\mathbf{e}^s \cdot \mathbf{e}^i) \text{ on } S_{int} \tag{4}$$

The topographic force arises from the traction induced by deformation at the boundaries of the domain (see Equation S5 in Souček et al., 2016). We form the topographic force by generating tractions on S_0 (i.e., $T_i^{t,0}$) and S_{int} (i.e., $T_i^{t,int}$). For small displacements, we can write $T_i^{t,int}$ and $T_i^{t,0}$ as a function of radial displacements at domain boundaries (i.e., $u_i(\mathbf{e}^i \cdot \mathbf{e}^s)$; note that here we only apply the Einstein summation convention for matching subscripts), ρ_{ice}, ρ_w, and gravitational acceleration at the inner and outer surfaces g_{int} and g_0 (see Table 2 in the main text):

$$T_i^{t,0} = u_i(\mathbf{e}^i \cdot \mathbf{e}^s)\rho_{ice} g_0(\mathbf{e}^s \cdot \mathbf{e}^i) \text{ on } S_0 \tag{5a}$$

$$T_i^{t,int} = u_i(\mathbf{e}^i \cdot \mathbf{e}^s)(\rho_{ice} - \rho_w) g_{int}(\mathbf{e}^s \cdot \mathbf{e}^i) \text{ on } S_{int} \tag{5b}$$

For the self-gravitational force, we evaluate a body force f_i^{sg} and a traction at the inner surface T_i^{sg}:

$$f_i^{sg} = \rho_{ice} \nabla V^{sg} \cdot \mathbf{e}^i \tag{6a}$$

$$T_i^{sg} = \rho_w V^{sg}(\mathbf{e}^i \cdot \mathbf{e}^s) \text{ on } S_{int} \tag{6b}$$

where V^{sg} is a gravitational potential arising from deformation (i.e., mass movement) at the boundaries of the domain. To compute V^{sg}, we combine solutions to the Poisson's equation (i.e., potentials) arising from boundary displacements (i.e., V^{sg}_{int} and V^{sg}_0) that are expanded into spherical harmonics (i.e., via the linear transformation H_{qw} where q and w are spherical harmonic degree and order). We evaluate potentials at radial locations r. $\mathcal{G}$ is the universal gravitational constant (i.e., as discussed in Hemingway & Mittal (2019) cf. Equation 4). We ignore effects due to the changes in density on V^{sg}:

$$V^{sg} = V^{sg}_{int} + V^{sg}_0 \tag{7}$$

$$V^{sg}_{int} = \sum_q \sum_w \frac{4\pi\mathcal{G}r}{2q+1}(\rho_w - \rho_{ice})\big(\frac{R_0}{r}\big)^{q+2} H_{qw} u_i(\mathbf{e}^i \cdot \mathbf{e}^s) \text{ on } S_{int} \tag{8a}$$

$$V^{sg}_0 = \sum_q \sum_w \frac{4\pi\mathcal{G}r}{2q+1}\rho_{ice}\big(\frac{r}{R_0 - \tilde{d}_{ice}}\big)^{q-1} H_{qw} u_i(\mathbf{e}^i \cdot \mathbf{e}^s) \text{ on } S_0 \tag{8b}$$

1.1.1.4 Fault Displacement

To consider the impact of frictionless faults in the crust (e.g., Tiger Stripes in *Faulted* models) on deformation, we assume that 2D fault surfaces within our geometry S_f are tractionless (i.e., dislocations fully cancel tidally-driven tractions evaluated along the fault plane). Following the formulation described in Segall, 2010 (Chapters 1-3), we relate displacements on either end of a fault surface (i.e., u^+_o and u^-_o where o is the displacement direction for nodes along a fault surface) to tractions T^f_i over S_f according to:

$$T^f_i = C_{ijkl} M_{klo} (u^+_o - u^-_o) n_j (\mathbf{e}^o \times \mathbf{e}^s) \text{ on } S_f \tag{9}$$

where M_{klo} is a rank-3 tensor containing linear Green's functions relating strike-slip motion to equivalent co-local strain along a fault plane in a 3D elastic medium (cf. Equation 3.23, Segall, 2010; Aki & Richards, 1980). Note that the addition of the cross term (i.e.,

$\mathbf{e}^o \times \mathbf{e}^s$) in Equation 9 ensures motion normal to fault surfaces does not contribute to traction induced by fault slip (i.e., fault surfaces are 'clamped' in the normal direction). We assume clamped fault surfaces (i.e., ignore mode-1 deformation from crack opening; Aagaard et al., 2007) based on the expectation that the magnitude of tidally-driven elastic extensional stresses within Enceladus's ice shell ($\sim$ 5-15 kPa; see Figure 1 of Behounkova et al., 2017) is much smaller than the average effective hydrostatic normal stresses across fault planes that are flooded by water ($\sim$ 120 kPa for *Faulted* models with $\tilde{d}_{ice} = 25$ km; see Equation S14 of Sládková et al., 2021). For models with lateral variations in thickness (i.e., LTV) and $\tilde{d}_{ice} \sim$ 15-17 km, we would expect that extensional stresses produced by diurnal would begin to approach the upper limit of mean effective hydrostatic stresses across the Tiger Stripes. We therefore acknowledge that mode-1 crack opening could occur across Tiger Stripes for relatively thin ice shells, but treating such a case is beyond the scope of the current work. We compute fault slip d_s by applying a rotation matrix R_{so} to transform vectors u_o^+ and u_o^- from the global cartesian coordinate system to a local fault coordinate system:

$$d_s = R_{so}(u_o^+ - u_o^-) \text{ on } S_f \tag{10}$$

1.1.2 Numerical Approximation and Solution Method

1.1.2.1 Weak Form of Equation of Motion

We construct the weak form of the quasi-static equation of motion by dotting the strong form of the equation of motion (Equation 1) with a weighting function ϕ_i:

$$\int_W (\sigma_{ij,j} + f_i)\ \phi_i\ dW = 0 \tag{11}$$

1.1.2.2 Galerkin Approach

Following the Galerkin approach, we formulate our weighting function ϕ_i as an n-dimensional combination of linear basis (i.e., shape) functions N^n scaled by coefficients c_i^n. We also formulate our trial solution (i.e., for displacement u_i) as an m-dimensional combination of linear basis functions N^m scaled by coefficients a_i^m:

$$\phi_i = \sum_n c_i^n N^n \tag{12a}$$

$$u_i = \sum_m a_i^m N^m \tag{12b}$$

1.1.2.3 Assembly of Jacobian

Considering the divergence theorem for stresses in W, substituting our formulation for the weighting function (Equation 12), and recognizing that the equation of motion's weak form is equivalent to the strong form for arbitrary weighting function coefficients c_i^n allows us to rewrite Equation 11 as:

$$-\int_W \sigma_{ij} N^n_{,j} dW + \int_S T_i N^n dS + \int_W f_i N^n dW = 0 \tag{13}$$

We substitute forces, stresses, and tractions from the constitutive relation (Equation 2), our tidal loading formulation (Equations 3, 4, 5, and 6), and our numerical treatment of fault surfaces (Equations 9 and 10) into Equation 13 to formulate a Jacobian A_{ij}^{nm}. A_{ij}^{nm} is a superposition of tensors integrated over our domain volume ${}_W A_{ij}^{nm}$, outer surface ${}_{S_0} A_{ij}^{nm}$, inner surface ${}_{S_{int}} A_{ij}^{nm}$, and fault sufraces ${}_{S_f} A_{ij}^{nm}$. We replace the linear transformation H_{qw} and the radial position of the domain r with the rank-4 tensor H_{qwnm} and the radial position of nodes r^n respectively:

$$A_{ij}^{nm} = {}_W A_{ij}^{nm} + {}_{S_0} A_{ij}^{nm} + {}_{S_{int}} A_{ij}^{nm} + {}_{S_f} A_{ij}^{nm} \tag{14}$$

$$
\begin{aligned}
{}_{W}A_{ij}^{nm} = \int_{V} (&\frac{1}{4}C_{ijkl}(N_{,k}^{m} + N_{,l}^{m})(N_{,j}^{n} + N_{,i}^{n}) + (\rho_{ice}\nabla(\sum_{q}\sum_{w}\frac{4\pi\mathcal{G}r^{n}}{2l+1}((\rho_{w}-\rho_{ice}) \\
&H_{qwnm}(\mathbf{e}^{i}\cdot\mathbf{e}^{s})\big(\frac{R_{0}}{r^{n}}\big)^{q+2} + \rho_{ice}H_{qwnm}(\mathbf{e}^{i}\cdot\mathbf{e}^{s})\big(\frac{r^{n}}{R_{0}-\tilde{d}_{ice}}\big)^{q-1}))\cdot\mathbf{e}^{j}))dW
\end{aligned}
\tag{15a}
$$

$$
\begin{aligned}
{}_{S_{int}}A_{ij}^{nm} = \int_{S_{int}} ((&\rho_{w}\sum_{q}\sum_{w}\frac{4\pi\mathcal{G}r^{n}}{2l+1}((\rho_{w}-\rho_{ice})H_{qwnm}(\mathbf{e}^{i}\cdot\mathbf{e}^{s})\big(\frac{R_{0}}{r^{n}}\big)^{q+2} + \rho_{ice}H_{qwnm} \\
&(\mathbf{e}^{i}\cdot\mathbf{e}^{s})\big(\frac{r^{n}}{R_{0}-\tilde{d}_{ice}}\big)^{q-1}))(\mathbf{e}^{s}\cdot\mathbf{e}^{j}) + (\mathbf{e}^{i}\cdot\mathbf{e}^{s})(\rho_{ice}-\rho_{w})g_{int}(\mathbf{e}^{s}\cdot\mathbf{e}^{j})N^{n}N^{m})dS
\end{aligned}
\tag{15b}
$$

$$
{}_{S_0}A_{ij}^{nm} = \int_{S_0} (\mathbf{e}^{i}\cdot\mathbf{e}^{s})\rho_{ice}g_{0}(\mathbf{e}^{s}\cdot\mathbf{e}^{j})N^{n}N^{m}dS \tag{15c}
$$

$$
{}_{S_f}A_{ij}^{nm} = \int_{S_f} C_{ijkl}M_{klo}(N_{o}^{m+} - N_{o}^{m-})n_{j}N^{n}dS \tag{15d}
$$

where N_o^{m+} and N_o^{m-} denote shape functions for split nodes on either side of a fault surface. We can also combine terms from Equations 3 and 4 to write a force vector b_j^n:

$$
b_{j}^{n} = -\int_{W}(\rho_{ice}\nabla V\cdot\mathbf{e}^{j})N^{n}dW - \int_{S_{int}}\rho_{w}V(\mathbf{e}^{s}\cdot\mathbf{e}^{j})N^{n}dS \tag{16}
$$

Finally, we assemble Equations 14, 15, and 16 to form a linear system and solve for displacement coefficients a_i^m.

$$
A_{ij}^{nm}a_{i}^{m} = b_{j}^{n} \tag{17}
$$

1.1.2.4 Solution Method

We solve Equation 17 using a multigrid method built into the PetSc solver package within Pylith (Aagaard et al., 2007). For the multigrid method, we apply preconditioners to A_{ij}^{nm} in Equation 17 to obtain solutions (i.e., coefficients a_i^m) for a series of increasingly fine mesh grids. We use Gaussian elimination to compute a_i^m for all grids except the coursest grid. To remove rigid body translational and rotational motion from solutions,

we apply singular-value decomposition and discard computed a_i^m values at the coursest grid level (for details, see 4.1.5 of Aagaard et al., 2007). We are able to mesh geometries, run simulations, and post-process model results for a single time step (e.g., at $t = 0$) within 60 – 90 minutes on a computer equipped with two CPU cores using our finite-element method.

1.2 Benchmarking

We benchmark our tidal loading formulation on *Base* models against analytic solutions using the spectral solver software package SATStress, a widely used tool within the planetary science community to predict diurnal (and fluid) Love number values and stress fields on planetary bodies (Wahr et al., 2009). SATStress solves the equation of motion for tidally-loaded multi-layered spherically symmetric bodies accounting for self-gravitation and viscous effects. Figure S1 shows predictions of Love number values from SATStress across our range of modelled $\tilde{d}_{ice}$ values. Within SATStress, we specify a multi-layered body with an outer ice layer and underlying ocean consistent with the rheological parameters in Table 2 (see main text), a mean ice viscosity 10^{16} Pa-s (Friedson & Stevenson, 1983), an ocean shear modulus 10^{-20} Pa, and an ocean viscosity 10^{-20} Pa-s. Love number values between numerical and analytical models agree to within <0.1% across all $\tilde{d}_{ice}$ values. Possible additional minor differences between predictions from either set of results may result from our lack of accounting for changes in ice shell rheology due to volumetric expansion or contraction within the ice shell during tidal loading (for details see Wahr et al., 2006).

We additionally compare model results from this work with results from Souček et al. (2016). Figure S2 shows displacement magnitude fields at three different time indices in

the tidal cycle (t=0.0 T (periapse), 0.2 T, and 0.4 T, where T is the orbital period $T = 33$ hrs) for models in Souček et al. (2016) (top row) and this work (bottom). We deactivate self-gravitation on *Base* models and assign weak zones with either 1. prescribed bulk modulus $\mu_{WZ} = 10^{-5}\mu$ and shear modulus $G_{WZ} = 10^{-5}G$ or 2. prescribed bulk modulus $\mu_{WZ} = \mu$ and shear modulus $G_{WZ} = 10^{-5}G$ to regions surrounding the Tiger Stripes for model comparisons. We find we are able to largely reproduce results from Souček et al., (2016) (i.e., peak displacement magnitude values correspond to within <10%) most accurately for models with both zero bulk and shear modulus. Discontinuities in radial displacement occur across all models with weak zones. Slight differences in displacement field characteristics persist surrounding the weak zone regions likely due to methodological differences in the implementation of adaptive mesh sizing, the assignment of reduced elastic moduli (i.e., the location of the Tiger Stripes and the shear modulus reduction away from fault planes), or the use of different shape functions (i.e., linear vs. quadratic) between models.

1.3 Mesh Convergence Test

We perform a mesh convergence test to confirm that Love number results from models with structural heterogeneities are not sensitive to chosen mesh sizing parameters. Figure S3 shows Love number values evaluated from models with only weak zones at chasma, Tiger Stripe, and circum-tectonic boundary locations (i.e., *WZ* models) and $\tilde{d}_{ice} = 15$ km meshed with specified minimum cell side lengths S_{min}= 6, 5, 4, 3, 2, and 1 km. We additionally show example snapshots of the radial displacement fields between our *WZ* model relative to our *Base* model for geometries with $\tilde{d}_{ice} = 15$ km across our range of tested S_{min} values. Results from Figure S3 demonstrate that both Love number results

and overall radial displacement fields are insensitive to chosen minimum cell size for values of $S_{min} < 3$ km. We accordingly assign $S_{min} = 1$ km for all models discussed in this work.

1.4 Choice of Weak Zone Elastic Parameters

We evaluate results from models with weak zones at chasma, Tiger Stripe, and circum-tectonic boundary locations (i.e., *WZ* models) to confirm that Love number outputs are not sensitive to our choice of weak zone shear modulus. Figure S4 shows Love number values evaluated from *WZ* models with $\tilde{d}_{ice} = 15$ km and specified weak zone moduli across $10^{-8} < G_{WZ}/G < 10^{0}$. We additionally show example snapshots of radial displacement fields from our *WZ* models relative to our *Base* model with $\tilde{d}_{ice} = 15$ km across our range of tested G_{WZ} values. Results from Figure S4 demonstrate that both Love number results and overall radial displacement fields are insensitive weak zone shear modulus for $G_{WZ}/G < 10^{-4}$. These results are consistent with those described in the supplementary documentation of Souček et al. (2016) but extend to inferences of displacement away from the Tiger Stripes and for instances of non-zero bulk modulus within weak zones.

1.5 Mode Coupling

We investigate the extent to which structural heterogeneities excite radial displacement patterns beyond degree-2 harmonics. For each model with structural heterogeneities, we treat radial displacement fields relative to the *Base* model (i.e., $u_r(\bar{\Omega})$, where $\bar{\Omega}$ is the position variable comprising the co-latitude longitude pair (θ, ϕ) in a reference frame fixed to Enceladus's center of mass). Note that $u^r(\bar{\Omega})$ is a sum over orthonormal spherical harmonic basis functions $Y_{lm}(\bar{\Omega})$ scaled by coefficients u^r_{lm} (l and m denote spherical

harmonic degree and order):

$$u^r(\bar{\Omega}) = \sum_{l=0}^{\infty} \sum_{m=-l}^{l} u^r_{lm} Y_{lm}(\bar{\Omega}) \tag{18}$$

The power of $u^r(\bar{\Omega})$ at a given spatial scale (i.e., l) can be represented via the power spectral density. We evaluate power spectral density using the root-mean-square of coefficients u^r_{lm} in Equation 18 over order m:

$$\text{Power Spectral Density} = \left(\frac{\sum_m (u^r_{lm})^2}{2l+1} \right)^{1/2} \tag{19}$$

Figure S5 shows power spectral density across l for *LTV*, *Faulted+LTV*, *Faulted*, *Faulted+ LTV+WZ*, and *WZ* models (See Figures 1 and 2 in the main text). Figure S5 demonstrates that structural heterogeneities stimulate mode coupling (i.e., non degree-2 deformation) across l = 2 - 20 with diminishing power at shorter wavelengths (i.e., higher l). Moreover, lateral variations in crustal thickness (i.e., in *LTV* and *WZ* models) and weak zones (i.e., in *WZ* and *Faulted + LTV + WZ* models) drive the most significant long-wavelength (l = 2 - 5) deformation across models. By contrast, deformation driven by faults (i.e., in *Faulted* models) is minimal at long-wavelengths but relatively more prominent at shorter wavelengths (l = 10 - 20) as compared to deformation in *LTV* models.

1.6 Ice Thickness and Thermal Thickness

We aim to describe the relationship between 1) the ice thickness $\tilde{d}_{ice}$ predicted from analyzing displacement over diurnal timescales at Enceladus and 2) the thermal thickness $\tilde{d}_t$ of ice between the surface and the water-ice phase transition at 273°K (i.e., the ice-ocean boundary). Note that the general (i.e., complex) form of the diurnal degree-2 shape Love number (for a spherically symmetric body) possesses both real $\Re(h^d_2)$ and imaginary $\Im(h^d_2)$ components. For a body that exhibits purely elastic deformation, $h^d_2 = \Re(h^d_2)$

and $\Im(h_2^d) = 0$. However, we expect the 'thermal' portion of the ice shell to exhibit an additional viscous component of deformation such that $\Im(h_2^d) \neq 0$. We can therefore estimate the ratio between $\tilde{d}_t$ and $\tilde{d}_{ice}$ by comparing $\Re(h_2^d)$ and $\Im(h_2^d)$:

$$\tilde{d}_t/\tilde{d}_{ice} = \frac{(\Im(h_2^d)^2 + \Re(h_2^d)^2)^{1/2}}{\Re(h_2^d)} \tag{20}$$

The imaginary Love number component $\Im(h_2^d)$ in Equation 20 is sensitive to the dynamic viscosity structure of the crust (Čadek et al., 2019). Viscosity $\eta(r)$ in the ice shell is a function of radial position r and $\tilde{d}_t$ (cf. Equations 56 and 57, Beuthe 2018):

$$\eta(r) = \eta_0 \cdot \exp\left(\frac{E}{R_g T_{io}}\left(\frac{T_{io}}{T_{io}^{(r-R)/(\tilde{d}_t)} T_s^{(r-R+\tilde{d}_t))/(\tilde{d}_t)}} - 1\right)\right) \tag{21}$$

where is $\eta_0 = 3{\cdot}10^{14}$ Pa-s is the minimum viscosity at the base of the ice shell (Čadek et al., 2019), $T_{io} = 273$ K and $T_s = 70$ K respectively are temperatures at the ice-ocean boundary and surface (Howett et al., 2010), $R = 252.1$ km is radius of the surface (Hemingway & Mittal, 2019), R_g is the gas constant, and $E = 59.4$ kJ mol^{-1} is the activation energy for diffusion creep of ice.

We solve for $\Im(h_2^d)$ and $\Re(h_2^d)$ using SATStress (Wahr et al., 2009, see also S1.2). Within SATStress, we specify a body with 100 equally thick layers of uniform rheology. For each layer, we linearly interpolate viscosity values from the radial viscosity structure described to Equation 21 and assign a constant shear modulus $G = 3.3$ GPa (Souček et al., 2016). Figure S6 shows results for computed $\Im(h_2^d)$, $\Re(h_2^d)$, and $\tilde{d}_t/\tilde{d}_{ice}$ (see Equation 20). Figure S6 demonstrates that $\tilde{d}_t/\tilde{d}_{ice} < 1.012$ for $\tilde{d}_t = 15 - 30$ km. In other words, estimates of mean ice thickness from Love numbers likely underestimate thermal thickness by less than $\sim 0.2\%$ at Enceladus (note that computed $\tilde{d}_t/\tilde{d}_{ice}$ are consistent with values expected when using complex Love numbers at Enceladus reported by Beuthe, 2018 cf. Figure 3).

1.7 Impact of Structural Heterogeneities on Horizontal Displacements

Results for horizontal displacement (i.e., orthogonal to the radial direction and tangential to the outer surface) across a range of model classes (see section 2.1 in the main text) are shown in Figure S7. Figure S7 demonstrates that the magnitude of horizontal displacements produced by structural heterogeneities are comparable to (or greater than) the magnitude of horizontal displacements in *Base* models near the South Pole of Enceladus (see discussion).

References

Aagaard, B., Williams, C., & Knepley, M. (2007). PyLith: A Finite-Element Code for Modeling Quasi-Static and Dynamic Crustal Deformation. *Eos*, *88(52)*.

Aki, K., & Richards, P. (1981). K. aki and p. g. richards 1980. quantitative seismology, theory and methods. volume i: 557 pp., 169 illustrations. volume ii: 373 pp., 116 illustrations. san francisco: Freeman. price: Volume i, u.s. 35.00; $volume ii, u.s.$35.00. isbn 0 7167 1058 7 (vol. i), 0 7167 1059 5 (vol. ii). *Geological Magazine*, *118*. doi: 10.1017/s0016756800034439

Behounkova, M., Soucek, O., Hron, J., & Cadec, O. (2017). Plume activity and tidal deformation on enceladus influenced by faults and variable ice shell thickness. *Astrobiology*, *17*(9). doi: 10.1089/ast.2016.1629

Beuthe, M. (2018). Enceladus's crust as a non-uniform thin shell: I tidal deformations. *Icarus*, *302*. doi: 10.1016/j.icarus.2017.11.009

Friedson, A. J., & Stevenson, D. J. (1983). Viscosity of rock-ice mixtures and applications to the evolution of icy satellites. *Icarus*, *56*. doi: 10.1016/0019-1035(83)90124-0

Hemingway, D. J., & Mittal, T. (2019). Enceladus's ice shell structure as a window on

internal heat production. *Icarus*, *332*. doi: 10.1016/j.icarus.2019.03.011

Howett, C. J., Spencer, J. R., Pearl, J., & Segura, M. (2010). Thermal inertia and bolometric bond albedo values for mimas, enceladus, tethys, dione, rhea and iapetus as derived from cassini/cirs measurements. *Icarus*, *206*. doi: 10.1016/j.icarus.2009.07.016

Segall, P. (2010). *Earthquake and volcano deformation*. doi: 10.5860/choice.48-0287

Sládková, K. P., Souček, O., & Běhounková, M. (2021). Enceladus' tiger stripes as frictional faults: Effect on stress and heat production. *Geophysical Research Letters*, *48*. doi: 10.1029/2021GL094849

Souček, O., Hron, J., Běhounková, M., & Čadek, O. (2016). Effect of the tiger stripes on the deformation of Saturn's moon Enceladus. *Geophysical Research Letters*, *43*(14). doi: 10.1002/2016GL069415

Wahr, Selvans, Z. A., Mullen, M. E., Barr, A. C., Collins, G. C., Selvans, M. M., & Pappalardo, R. T. (2009). Modeling stresses on satellites due to nonsynchronous rotation and orbital eccentricity using gravitational potential theory. *Icarus*, *200*(1). doi: 10 .1016/j.icarus.2008.11.002

Wahr, Zuber, M. T., Smith, D. E., & Lunine, J. I. (2006). Tides on Europa, and the thickness of Europa's icy shell. *Journal of Geophysical Research E: Planets*, *111*(12). doi: 10.1029/2006JE002729

Čadek, O., Souček, O., Běhounková, M., Choblet, G., Tobie, G., & Hron, J. (2019). Long-term stability of enceladus' uneven ice shell. *Icarus*, *319*. doi: 10.1016/j.icarus .2018.10.003

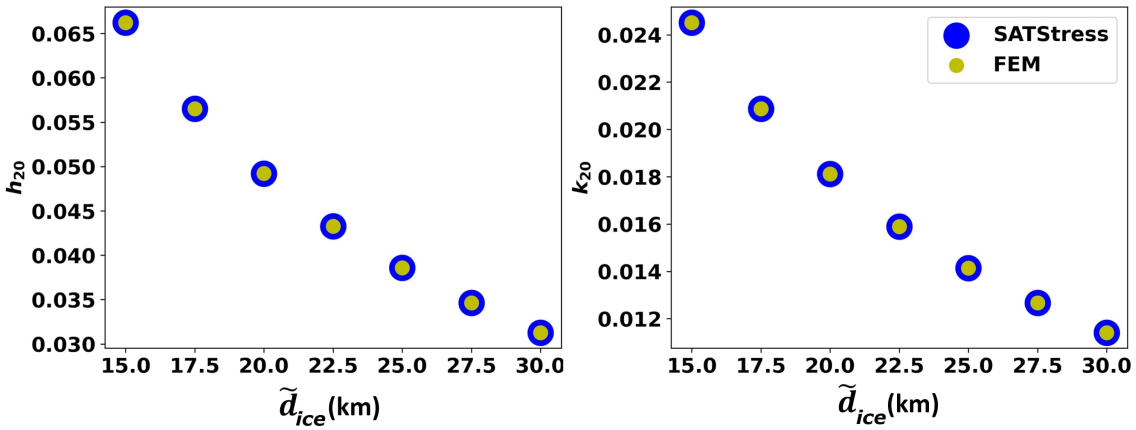

Figure S1. Comparison of analytic and FEM Love number results for several values of $\tilde{d}_{ice}$ on spherically symmetric (*Base*) models. Love numbers plotted against $\tilde{d}_{ice}$ for analytic models using SATStress (blue dots) and using the FEM formulated here (yellow dots).

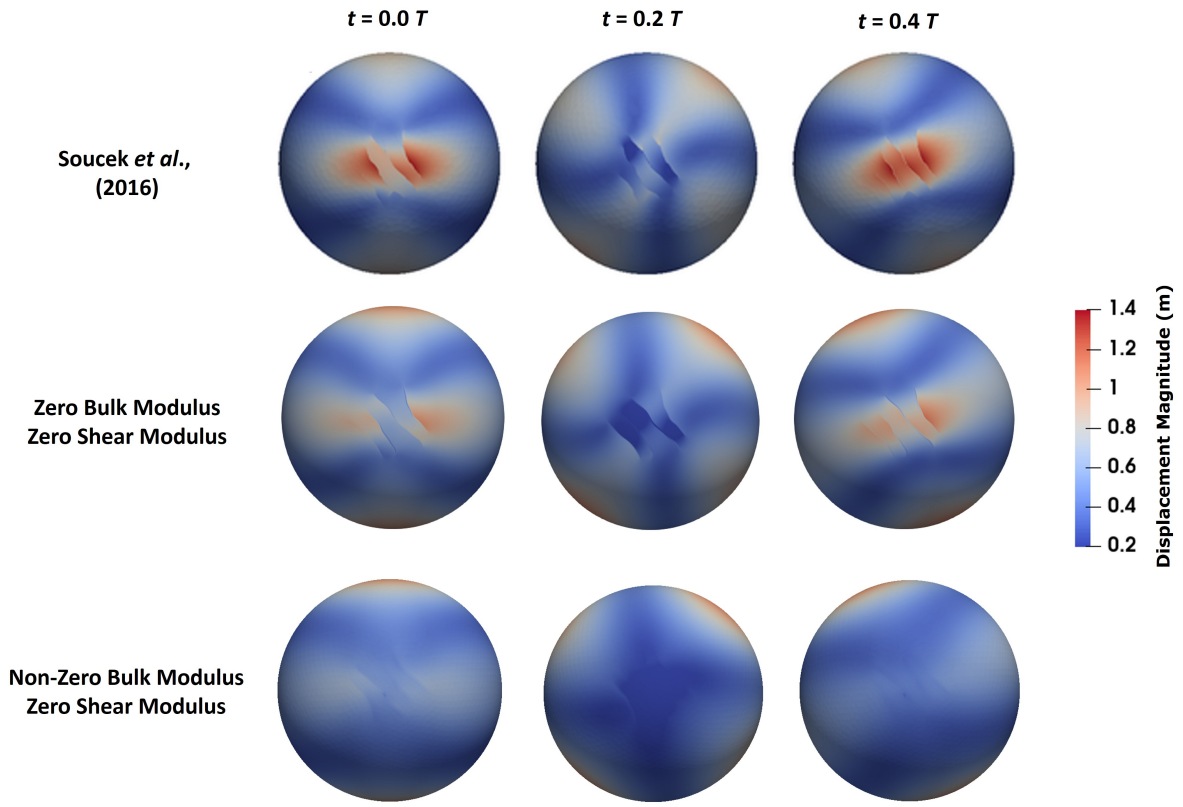

Figure S2. Comparison of results from models with Tiger Stripes in Souček et al. (2016) (top row) with results from models which employ weak zones with effectively zero bulk modulus and effectively zero shear modulus (center row) as well as non-zero bulk modulus and effectively zero shear modulus (bottom row) at Tiger Stripe locations. Models are viewed facing the South Pole. Fields denote the magnitude of the displacement vector evaluated at the outer surface of deformed geometries. The top row and colorbar of this Figure are adapted from top row of Figure 3 of Souček et al. (2016).

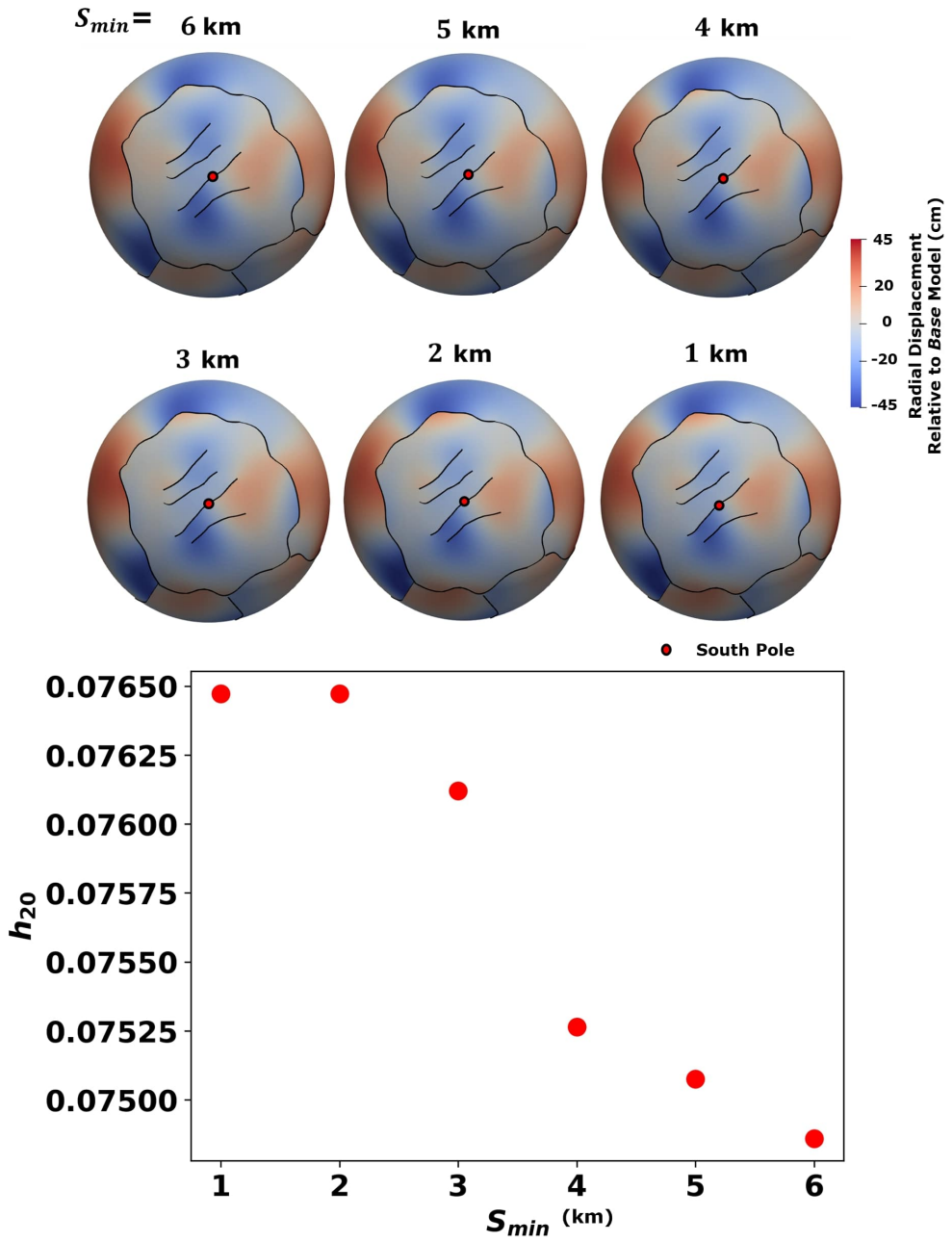

Figure S3. Results evaluated at periapse for WZ models ($\tilde{d}_{ice} = 15$ km) for a range of S_{min}. We show radial displacement fields viewed facing upwards towards the South Pole (top) and h^d_{20} Love number results we use to track the sensitivity of results due to changes in S_{min} (bottom)

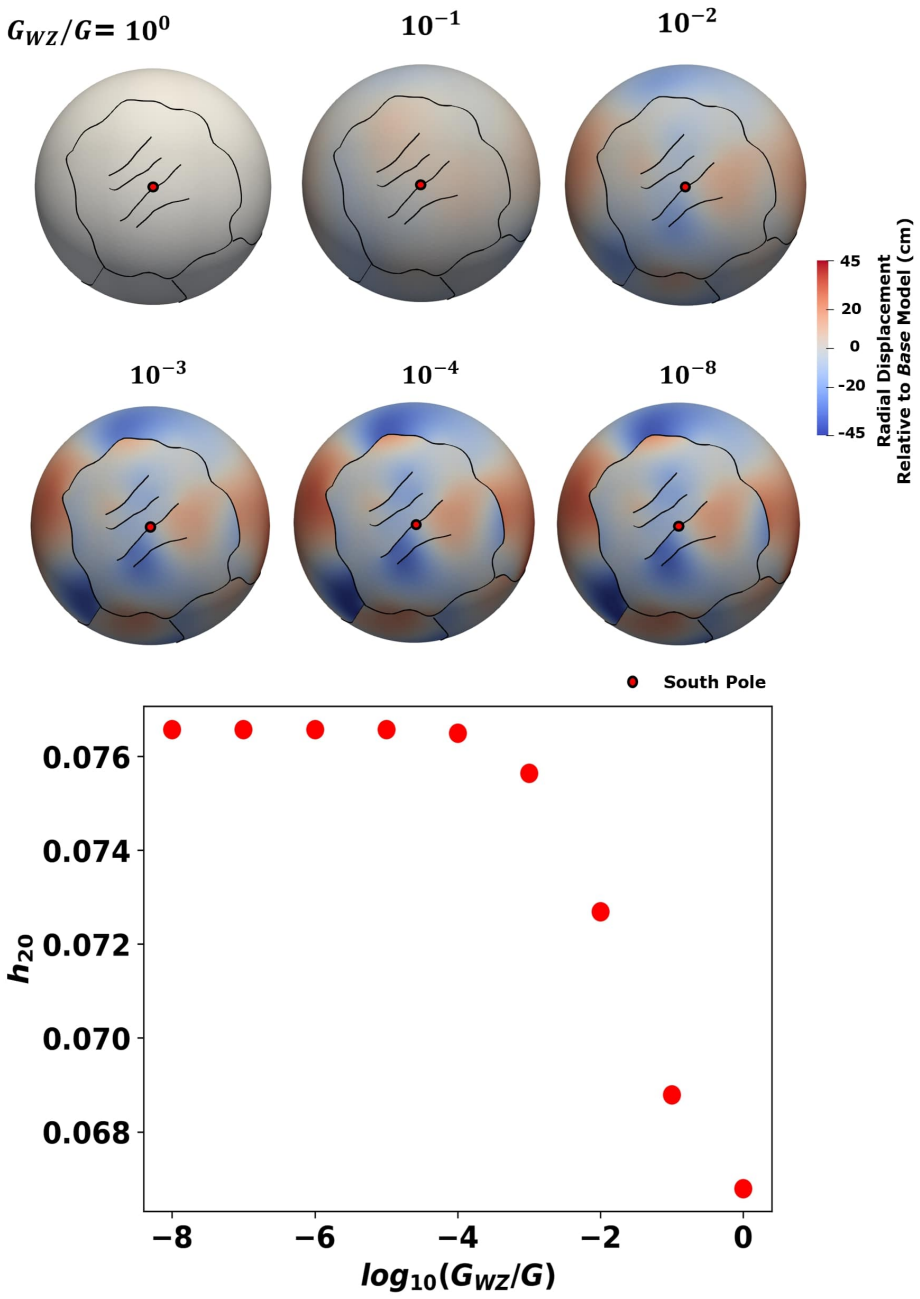

Figure S4. Results evaluated at periapse for WZ models ($\tilde{d}_{ice} = 15$ km) across several values of G_{WZ}. We show radial displacement fields viewed facing upwards towards the SP (top) and h^d_{20} Love number results we use as a proxy for effective model stiffness.

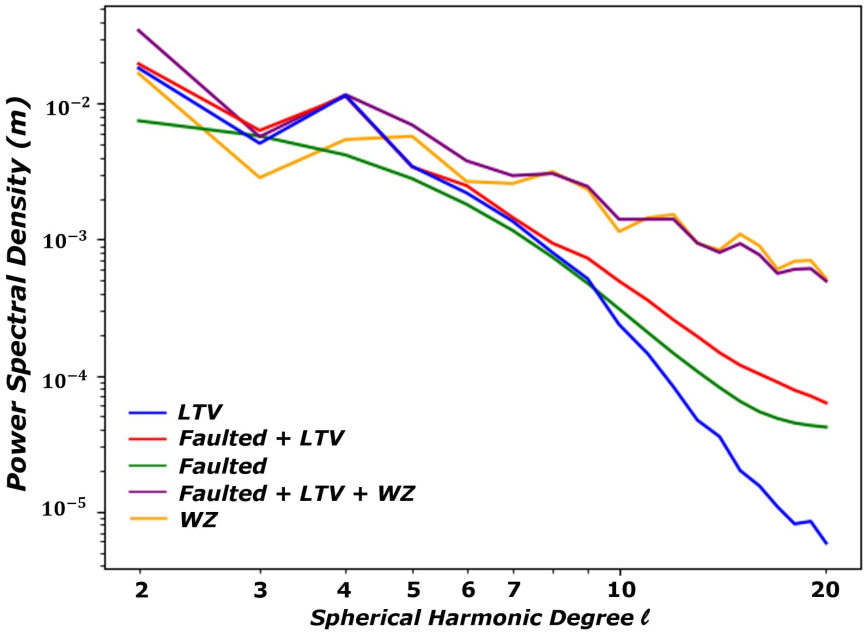

Figure S5. Power spectral density of surface radial displacements for models with structural heterogeneities described in this work. We compute power spectral density for each model using Equations 18 and 19. For a description of each model class, see section 2.1 of the main text. Axes are plotted in $\log_{10}$ scale.

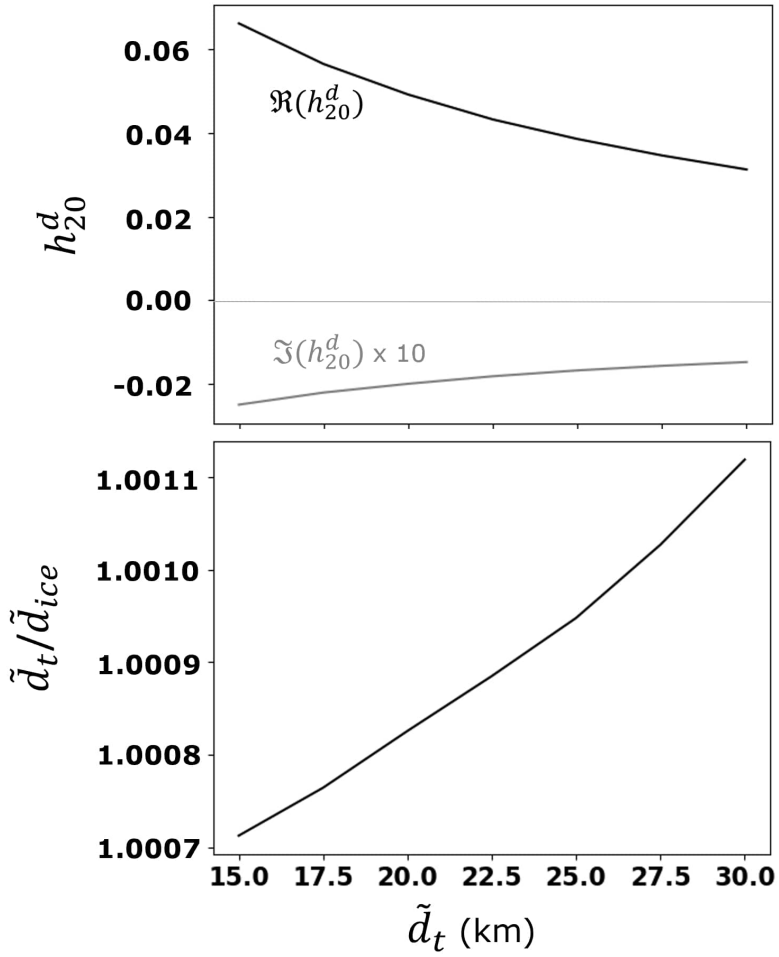

Figure S6. Computed complex Love number components $\Im(h_2^d)$ and $\Re(h_2^d)$ (top row), and associated $\tilde{d}_t/\tilde{d}_{ice}$ values (see Equation 20) (bottom row) across input mean crustal thicknesses $\tilde{d}_t$ = 15-30 km. We evaluate $\Im(h_2^d)$ and $\Re(h_2^d)$ using SATStress and following the procedure described in S1.6.

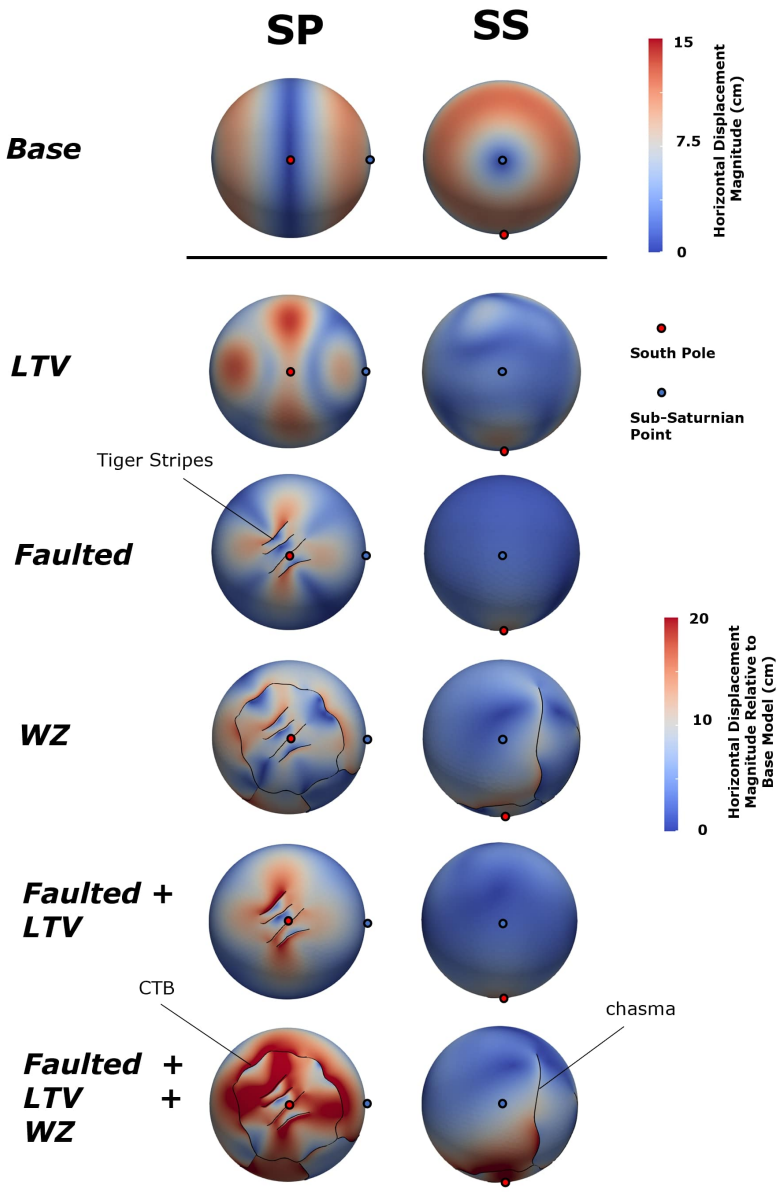

Figure S7. Snapshots of the magnitude of horizontal displacement from each model class viewed facing the south pole (SP, left column) and the sub-Saturnian point (SS, right column) evaluated at $t = 0$ (periapse). The top row shows the magnitude of horizontal displacement in the *Base* model due to tidal forcing. The remaining rows present the magnitude of the difference in horizontal displacement between models with structural heterogeneities and the *Base* model. Each model shown assumes $\tilde{d}_{ice} = 25$ km. Tiger Stripes, the south polar circum-tectonic boundary (CTB), and chasma are labelled.

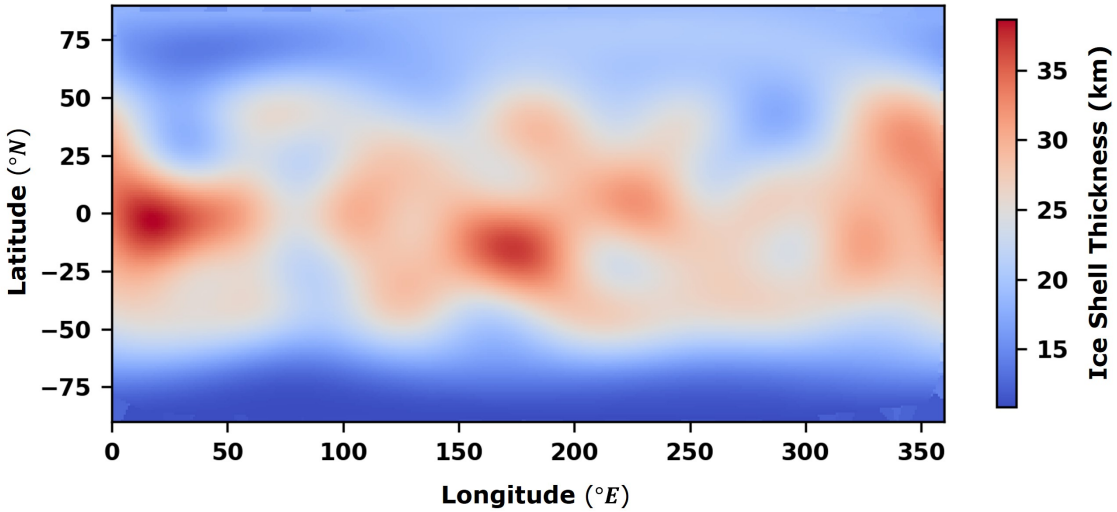

Figure S8. Crustal thickness variations for LTV models. For details regarding our methodology to generate crustal thickness variations, see section 2.1 of the main text.